THE JOURNAL OF PHYSICAL CHEMISTRY C
A JOURNAL OF THE AMERICAN CHEMICAL SOCIETY

pubs.acs.org/JPCC

Article

Mechanism of the Cluster-Mediated Fe^{2+} Delivery through Carbon Nanoparticle Suspension Injection (CNSI) for Ferroptosis-Based Cancer Therapy: A Dual Experimental/Molecular Dynamics Simulation Study

Shiga Jila,[‖] Cheng Zeng,[‖] Kexin Tang, Ping Xie, Huahui Yuan, Chunchun Zhang, Junxian Chen,* Sheng-Tao Yang,* and Xiaohai Tang*

Cite This: *J. Phys. Chem. C* 2025, 129, 22526−22537

Read Online

ACCESS | Metrics & More | Article Recommendations | Supporting Information

ABSTRACT: Excessive Fe^{2+} accumulation in tumors has been extensively studied as a target for ferroptosis-based cancer therapy. A carbon nanoparticle−Fe(II) complex through suspension injections (CNSI−Fe) has been established as a delivery system of Fe^{2+} for tumor inhibition through ferroptosis. However, it is still largely unknown about the Fe^{2+} delivery mechanism through CNSI, which is critically urgently needed for the clinical trials of CNSI−Fe. Herein, the Fe^{2+} delivery mechanism is derived by combining theoretical and experimental investigations in comparison with the Cu^{2+} the Zn^{2+} adsorption by CNSI. The similarity is that all three metal ions undergo heterogeneous chemisorption through hydrogen bonds formed between the oxygen-containing groups of CNSI and the coordination water of the metal ions. The differences lie in the fact that CNSI exhibits cluster-mediated adsorption for Fe^{2+}, multilayer adsorption for Cu^{2+}, and primarily single-layer adsorption with loose ion stacking for Zn^{2+}. The formation of Fe^{2+} clusters is attributed to the bidentate coordination of SO_4^{2-} with Fe^{2+}, so the hydrogen bonds between the outer-layer SO_4^{2-} of the Fe^{2+} clusters and the oxygen-containing groups of CNSI also contribute to Fe^{2+} delivery. This unique Fe^{2+} delivery mechanism, mainly based on the acidic formulation and mesoporous characteristics, makes CNSI−Fe highly valuable for clinical ferroptosis-based cancer therapy.

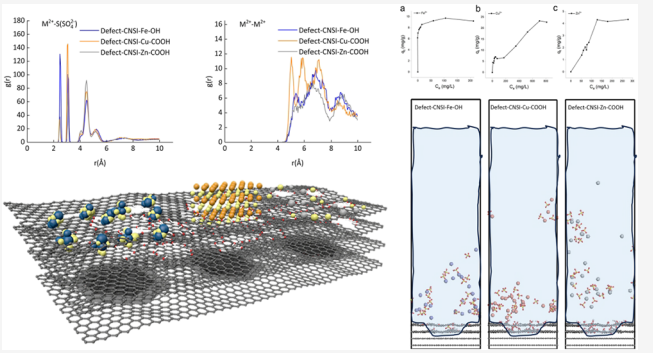

INTRODUCTION

Excessive iron accumulation in tumors arouses intense oxidative stress and initiates ferroptosis. This phenomenon has been adopted for cancer therapy, where Fe-containing nanoparticles (NPs) are considered an emerging nanomedicine for ferroptosis-based cancer therapy. For instance, Wang et al. modified ferrous sulfide NPs with a carbonic anhydrase inhibitor (CAI) to release CAI, Fe^{2+}, and H_2S, which initiated the Fe^{2+}-mediated Fenton reaction to start ferroptosis for efficient tumor inhibition.[1] In Liang et al.'s investigation, the renal clearable ultrasmall single-crystal Fe NPs were effective in inducing immunogenic cell death and tumor cell ferroptosis.[2] A near-infrared (NIR) light-triggered Fe^{2+} delivery agent (LET-6) was disclosed by He et al.[3] When NPs were exposed to laser irradiation, their thermal expansion caused LET-6 to release Fe^{2+}. Li et al. delivered Fe^{2+} via metal−organic framework ZIF-8 NPs, where the ferroptosis stopped MDA-MB-231 cells and tumors from growing.[4] However, Fe-containing NPs face lots of challenges, such as complex formulation, difficulty in large-scale manufacture, and batch-to-batch variability, as well as crucial toxicity and safety problems for clinical applications. Beyond the common challenges faced by nanomedicine, the major challenge for Fe-containing NPs in ferroptosis-based cancer therapy is releasing enough Fe^{2+} in a short time to reach an effective concentration.

Alternatively, recent progress has been made in the field of microextraction of heavy metal ions using carbonaceous materials, on which there are many oxygen-containing groups (OG) to interact with metal ions.[5] Among those promising carbon nanomaterials, carbon nanoparticle suspension injection (CNSI), also known as Canarine, is the only commercially and clinically utilized carbon nanomaterial. CNSI is mainly applied in staining the tumor drainage lymph node black after intratumoral injection during surgery.[6,7] Experimental and clinical studies have proven the

Received: August 28, 2025
Revised: November 27, 2025
Accepted: December 1, 2025
Published: December 10, 2025

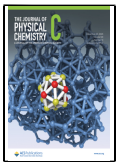

https://doi.org/10.1021/acs.jpcc.5c05997
J. Phys. Chem. C 2025, 129, 22526−22537

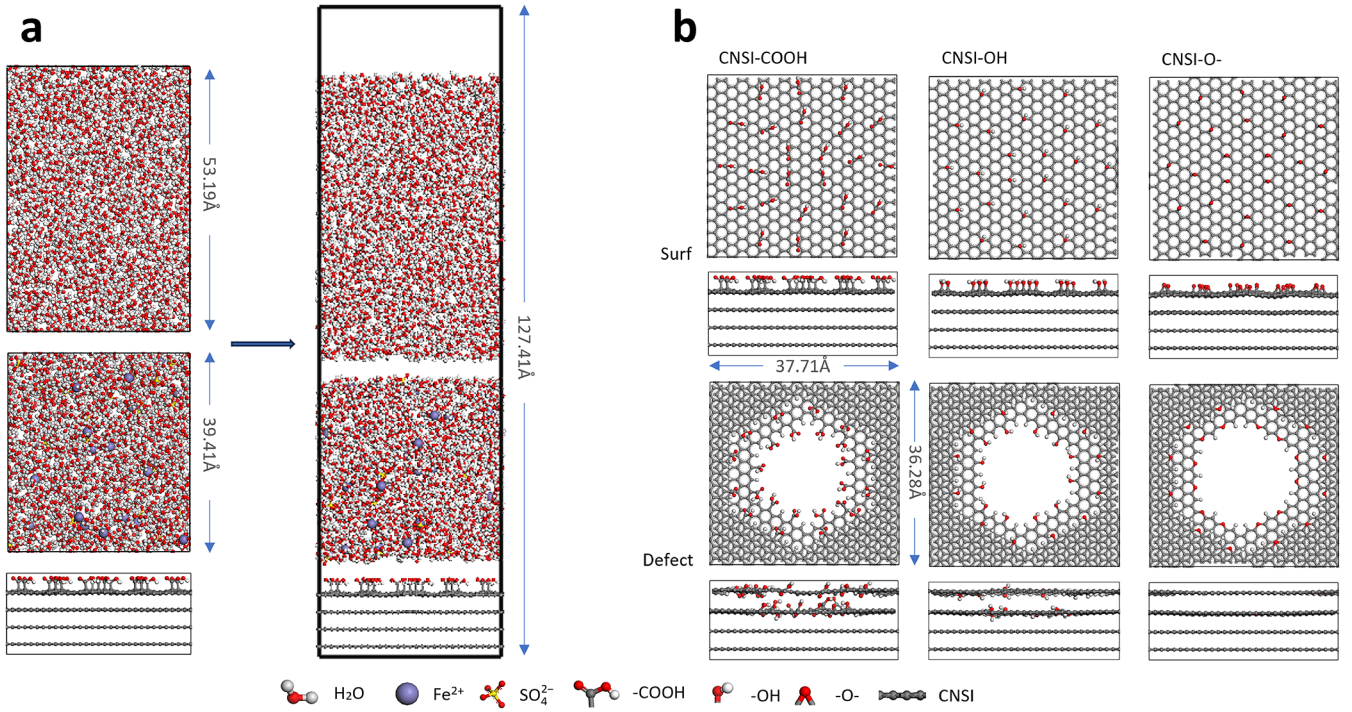

Figure 1. Specification of the surface and defect systems (a) and the oxidized carbon surface and defect layers with the distribution of their oxygen-containing group (b).

biosafety of CNSI.[8,9] Moreover, CNSI also finds new applications in other biomedical areas, such as drug carriers, photothermal therapy, and immune adjuvants.[10−13] When CNSI is simply mixed with Fe^{2+} ions, the CNSI−Fe complex could be easily prepared as a black suspension.[14] CNSI−Fe could efficiently load Fe^{2+} into tumor cells, which demonstrated high antitumor efficiency. The intratumoral injection of CNSI−Fe resolved the Fe^{2+} buildup issue in the tumor, and the good biosafety of carbon enabled its safe use. CNSI−Fe has been established in the ferroptosis-based therapy of multiple tumor models.[14,15] CNSI−Fe has been approved for clinical trials (National Medical Products Administration's Center for Drug Evaluation: No. CTR20222235) and is currently under the evaluation of the Phase II trial. However, it is still not clear how CNSI effectively delivers and releases Fe^{2+} after intratumoral injection. The lack of a delivery mechanism of Fe^{2+} by CNSI largely hinders the clinical application and commercialization of CNSI−Fe. Therefore, it is crucial to thoroughly investigate the delivery mechanism of CNSI−Fe at the molecular level.

Molecular dynamics (MD) simulations provide dynamic and high-resolution details, which are instrumental in gaining a deep understanding of the adsorption and delivery properties of carbon nanomaterials.[16,17] For example, Tang et al. investigated the adsorption of aromatic compounds on graphene oxide (GO), where theoretical calculation demonstrated that the adsorption capacity was mainly guided by the π-stacking ability of aromatic compounds.[18] Hou et al. studied the structural, dynamical, and interfacial behavior of calcium and sulfate ions in the vicinity of the GO sheet and pointed out the effects of surface properties on the behavior of ions and four surface types.[19] However, there are almost no MD studies of the adsorption and interaction of Fe^{2+} by carbon nanomaterials.

In this study, we aimed to explore the delivery mechanism of Fe^{2+} by CNSI in the ferroptosis-based cancer therapy by CNSI−Fe. Experimental approaches were carried out to characterize the structures and functional groups of CNSI−Fe and measure the adsorption behaviors of Fe^{2+}, Cu^{2+}, and Zn^{2+} on CNSI. Based on the characteristics of CNSI and the acidic environment of the CNSI−Fe system, surface and defect oxidation models were constructed for the CNSI−Fe, CNSI−Cu, and CNSI−Zn systems. Combining with the experimental results, the similarities and differences of MD simulations were analyzed at the atomic/molecular level to elucidate the Fe^{2+} delivery mechanism. Further, the implications for the clinical applications of CNSI−Fe are discussed.

MATERIALS AND METHODS

Adsorption Experiments. CNSI was provided by Chongqing Lummy Pharmaceutical Co., Ltd. and carefully characterized (Supporting Information). CNSI and different amounts of Fe^{2+}, Cu^{2+}, and Zn^{2+} solutions were mixed, and the volume was fixed with aqueous hydrochloric acid solution (pH 3.0). The adsorption was carried out by a vapor-bath shaker at 37 °C and 110 rpm for different times of oscillation to reach equilibrium. Then, an appropriate amount of the solution was taken out, added to a 30 kDa ultrafiltration tube, and centrifuged at 4000 rpm for 10 min. The filtrate was subjected to different complexation reactions and was fixed to a volume. Finally, the concentrations of Fe^{2+}, Cu^{2+}, and Zn^{2+} solutions (C_t at different time points and C_e at 180 min) were determined by a UV−vis spectrophotometer at 510, 455, and 620 nm, respectively. Please refer to the Supporting Information for specific reagents, apparatus, and solution configurations.

Equation 1 was used for the calculation of the adsorption capacity. The adsorption kinetics data for Fe^{2+}, Cu^{2+}, and Zn^{2+} adsorption were treated with the following pseudo-first-order[20]

https://doi.org/10.1021/acs.jpcc.5c05997
J. Phys. Chem. C 2025, 129, 22526−22537

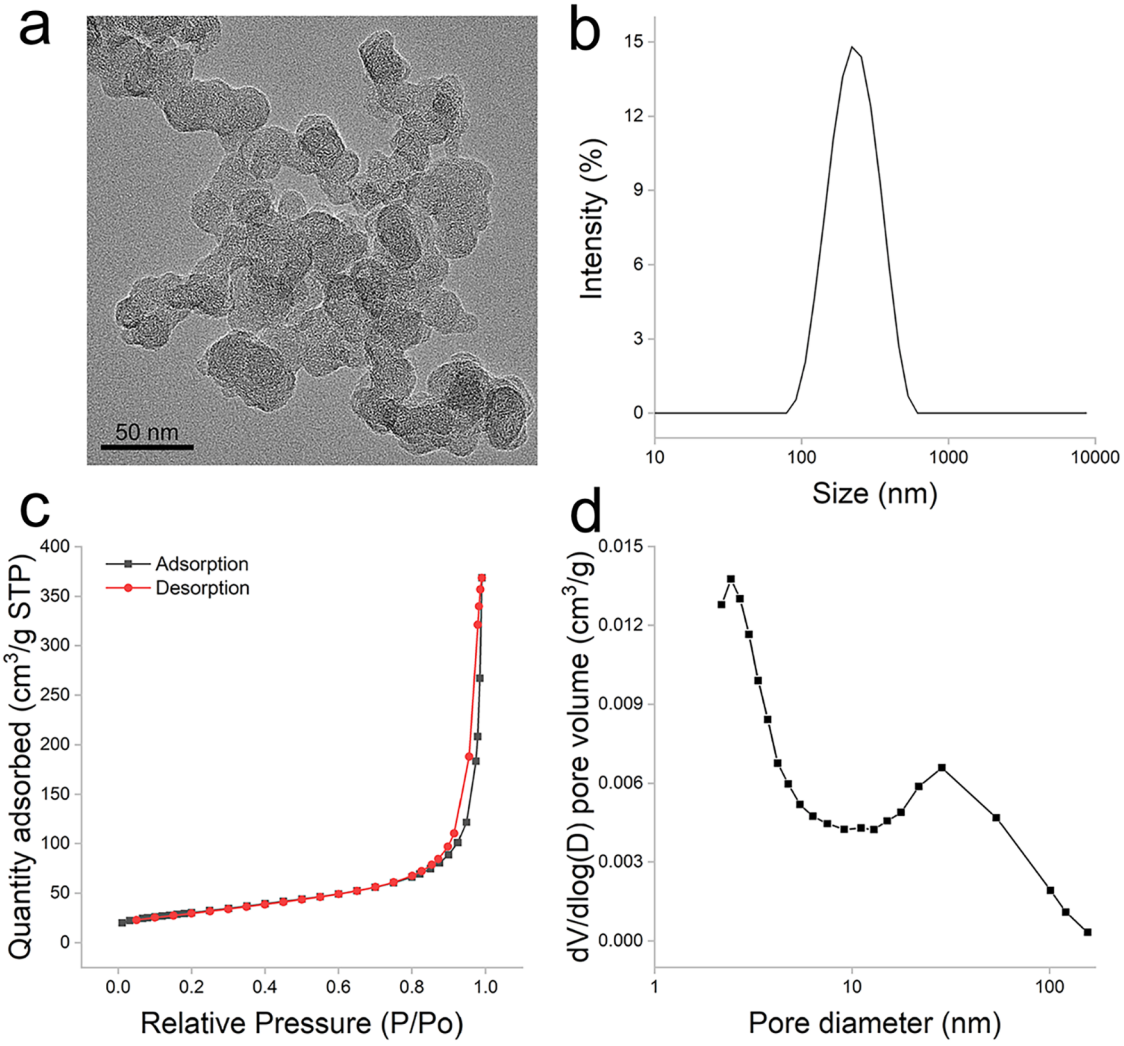

Figure 2. Characterization of starting material C40 in CNSI. (a) TEM image of C40, (b) dynamic light scattering (DLS) particle size distribution of CNSI, (c) N_2 adsorption/desorption isothermal curve of C40, and (d) pore size distribution of C40.

(eq 2) and pseudo-second-order[21] models (eq 3) in linear forms:

$$q_t = \frac{(C_o - C_t)V}{m} \tag{1}$$

$$\ln(q_e - q_t) = \ln q_e - k_1 t \tag{2}$$

$$\frac{t}{q_t} = \frac{1}{k_2 q_e^2} + \frac{t}{q_e} \tag{3}$$

where q_t (mg·g^{-1}) and q_e (mg·g^{-1}) are the adsorption amount at moment t and the equilibrium adsorption capacity, respectively; C_0 (mg·L^{-1}) and C_t (mg·L^{-1}) are the initial concentration and the concentration at moment t of metal ions, respectively; V (mL) is the solution volume; m (g) is the amount of the CNSI adsorbent; t (min) is the time; k_1 (min^{-1}) is rate constant of the pseudo-first-order model, and k_2 (g·mmol^{-1}·min^{-1}) is rate constant of the pseudo-second-order model.

The isothermal adsorption data were fitted with the Langmuir model[22] (eq 4), the Freundlich model[23] (eq 5), and the Temkin model[24] (eq 6).

$$q_e = \frac{q_m K_L C_e}{1 + K_L C_e} \tag{4}$$

$$q_e = K_F C_e^{1/n} \tag{5}$$

$$q_e = B \ln A + B \ln C_e \tag{6}$$

where q_m (mg·g^{-1}) is the maximum adsorption capacity, C_e (mg·L^{-1}) is the concentration of metal ions at equilibrium, Langmuir's constant K_L (L·mg^{-1}) is related to the energy of adsorption, Freundlich's constant K_F (mg·g^{-1})·(mg·L^{-1})$^{-1/n}$ is indicative of the relative adsorption capacity of the adsorbent, the linear exponent n is lying in the range of 1−10 for classification as favorable adsorption, Temkin's constant B (mg·g^{-1}) is about the variation of adsorption energy, and A (mg·L^{-1}) is the equilibrium binding constant.

MD Modeling and Method. According to the acidic formulation of CNSI−Fe, the oxygen-containing groups only included carboxyl (−COOH), hydroxyl (−OH), and epoxy (−O−).[25] Both models were built by a water box with 2400 H_2O molecules, an $FeSO_4$ solution box with 24 Fe^{2+} ions, 24 SO_4^{2-} ions, and 1600 H_2O molecules, and a carbon box with three 37.71 × 36.28 Å^2 graphene layers with 24 oxidized groups (Figure 1). For the surface, only the top layer was oxidized,

https://doi.org/10.1021/acs.jpcc.5c05997
J. Phys. Chem. C 2025, 129, 22526−22537

while for the three defect layers, the upper two layers were excavated with two sizes of hexagonal holes, whose side lengths were 8 and 6 times the width of benzene, respectively. As a result, three surface systems and three defect systems were built: Surf−CNSI−Fe−COOH, Surf−CNSI−Fe−OH, Surf−CNSI−Fe−O−, defect−CNSI−Fe−COOH, defect−CNSI−Fe−OH, and defect−CNSI−Fe−O− systems. Similarly, 12 CNSI−Cu and CNSI−Zn models were built.

All water boxes and $FeSO_4$ solution boxes were optimized, followed by 200 ps NVT and 200 ns NPT MD simulations before they were included in the systems. Then, all the systems were reoptimized and run 500 ps equilibration at the NVE ensemble. At last, they were performed in the NVT ensemble for 5 ns to prepare the final analysis. All the MD simulations were performed with the COMPASS force field[26] using the Forcite module of the Materials Studio 2008 programs.[27] Time steps and temperatures were 1 fs and 300 K, respectively. The Berendsen thermostat and barostat were applied to control the temperature and pressure, respectively.[28] The long-range electrostatic forces were calculated through the Ewald summation routine.[29]

RESULTS AND CONCLUSIONS

Characterization of CNSI. C40, the starting material of the CNSI, showed a diameter of 20.4 nm under transmission electron microscopy (TEM) (Figure 2a). Due to $\pi-\pi$ interactions and hydrophobic interactions, significant aggregation of carbon NPs occurred during the preparation of CNSI suspension, which was reflected by the hydrodynamic diameter of 211.8 ± 3.0 nm (Figure 1b). In the N_2 adsorption/desorption isothermal curves of C40, the adsorption curves during pressure increase and the desorption curves during pressure decrease did not overlap, but formed a mesoporous hysteresis loop, which was assigned to a type IV isotherm of the H1b-type hysteresis loop (Figure 2c). The specific surface area of C40 was 107.7 $m^2 \cdot g^{-1}$ and the pore volume was 0.41 $cm^3 \cdot g^{-1}$, as measured by Brunauer−Emmett−Teller (BET). The pore size distribution was mainly at 28 nm (Figure S1d). Compared to C40, there was a decrease in the oxygen content after making the CNSI suspension (Table S1) from 4.60 to 2.49%, a reduction of 2.11%. These results collectively indicated the presence of mesopores with large pore sizes and oxygen-containing groups on CSNI, which served as the basis for the construction of the defect model (Figure 1).

Adsorption of Metal Ions on CNSI. Figure S1 presents the adsorption kinetics of Fe^{2+}, Cu^{2+}, and Zn^{2+} by CNSI, showcasing the time-dependent behavior of the adsorption process. The adsorption of ions reached 90% of the equilibrium adsorption within 30 min, and a slow increase was observed at the later stage. Therefore, the adsorption time of CNSI for metal ions was considered to be 30 min. The pseudo-first-order model and the pseudo-second-order model of adsorption kinetics were fitted at intermediate concentrations. The relevant parameters of adsorption kinetics are listed in Table 1. The R^2 values of the pseudo-second-order kinetic model (>0.99) were higher than those of the pseudo-first-order kinetic model, indicating that the pseudo-second-order kinetic model better fitted the adsorption kinetic data of three metal ions. Moreover, the $q_e^{cal}(Fe^{2+})$ of 9.38 $mg \cdot g^{-1}$, $q_e^{cal}(Cu^{2+})$ of 6.79 $mg \cdot g^{-1}$, and $q_e^{cal}(Zn^{2+})$ of 1.79 $mg \cdot g^{-1}$ fitted by the quasi-second-order kinetic model were very close to the measured values of $q_e^{exp}(Fe^{2+})$ of 9.24 $mg \cdot g^{-1}$, $q_e^{exp}(Cu^{2+})$ of 6.70 $mg \cdot g^{-1}$, and $q_e^{exp}(Zn^{2+})$ of 1.73 $mg \cdot g^{-1}$, further demonstrating the applicability of this model. The pseudo-second-order kinetic model is suitable for describing the complex dynamic behavior of the adsorption process, which not only takes into account the physical diffusion process but also emphasizes the dominant role of chemisorption.[30,31] On the other hand, the pseudo-second-order adsorption rate constants $k_2(Fe^{2+}) \ll k_2(Zn^{2+}) < k_2(Cu^{2+})$ indicated that the adsorbent CNSI adsorbed Cu^{2+} at the fastest rate and Fe^{2+} at a slowest rate. However, the Fe^{2+} adsorption rate is significantly lower than those of the other two, suggesting that the adsorption characteristics of the CNSI−Fe system differ from those of the other two.

Table 1. Parameters of Adsorption Kinetics and Isotherms for the Adsorption of Fe^{2+}, Cu^{2+}, and Zn^{2+} by CNSI

model	parameter	Fe^{2+}	Cu^{2+}	Zn^{2+}
	q_e^{exp}, $mg \cdot g^{-1}$	9.24	6.70	1.73
pseudo-first-order	R^2	0.9805	0.1660	0.5200
	k_1, min^{-1}	0.0215	0.0001	0.0009
	q_e^{calc}, $mg \cdot g^{-1}$	10.23	16.05	2.92
pseudo-second-order	R^2	0.9992	0.9997	0.9996
	k_2, $g \cdot mmol^{-1} \cdot min^{-1}$	0.028	0.167	0.137
	q_e^{calc}, $mg \cdot g^{-1}$	9.38	6.74	1.79
Langmuir	R^2	0.5427	0.8096	0.8402
	K_L, $L \cdot mmol^{-1}$	5.025	0.003	0.005
	q_m, $mg \cdot g^{-1}$	8.80	30.01	8.22
Freundlich	R^2	0.9102	0.9100	0.7896
	$1/n$	0.056	0.493	0.600
	K_F, $mg^{1+1/n} \cdot g^{-1} \cdot L^{-1/n}$	7.185	0.824	0.168
Temkin	R^2	0.9152	0.8034	0.8654
	ln A	15.244	−2.500	−3.240
	B, $mg \cdot g^{-1}$	0.468	4.760	2.046

Figure S2 shows the experimental isothermal adsorption curves for the CNSI−Fe, CNSI−Cu, and CNSI−Zn systems, revealing the relationship of maximum adsorption capacities q_m (Cu^{2+}, 22.7 $mg \cdot g^{-1}$) > q_m (Fe^{2+}, 9.2 $mg \cdot g^{-1}$) > q_m (Zn^{2+}, 4.3 $mg \cdot g^{-1}$). Notably, the adsorption isotherm of CNSI for Cu^{2+} followed a typical BET multilayer adsorption model.[32−34] The flatter region in the middle represents the formation of a monolayer. At the knee, monolayer formation began and multilayer formation occurred at medium concentrations. At higher concentrations, capillary condensation occurred. This not only explained why CNSI had a much higher q_m for Cu^{2+} than for the other two metal ions but also explained why the adsorption rate constant k_2 of the pseudo-second-order model for CNSI−Cu was negative.

The fitting curves of the Langmuir, Freundlich, and Temkin isotherm adsorption models for the three ions are shown in Figure S3, and the related fitting parameters are listed in Table 1. The R^2 value of the Freundlich model (0.9100) indicated that the Freundlich model was more suitable for describing the Cu^{2+} adsorption by CNSI than those of the Langmuir model (0.8096) and Temkin model (0.7994), indicating that it was a multilayer heterogeneous adsorption.[35,36] For Zn^{2+} adsorption, the Temkin and Langmuir models fitted relatively well, although their R^2 values are only 0.865 and 0.840, respectively, implying that the adsorption behavior was closer to single-layer heterogeneous adsorption.

However, the isothermal fitting indicates that single-layer adsorption did not apply to the adsorption of Fe^{2+} by CNSI, with a Langmuir R^2 value of only 0.5427. In contrast, the R^2

https://doi.org/10.1021/acs.jpcc.5c05997
J. Phys. Chem. C 2025, 129, 22526−22537

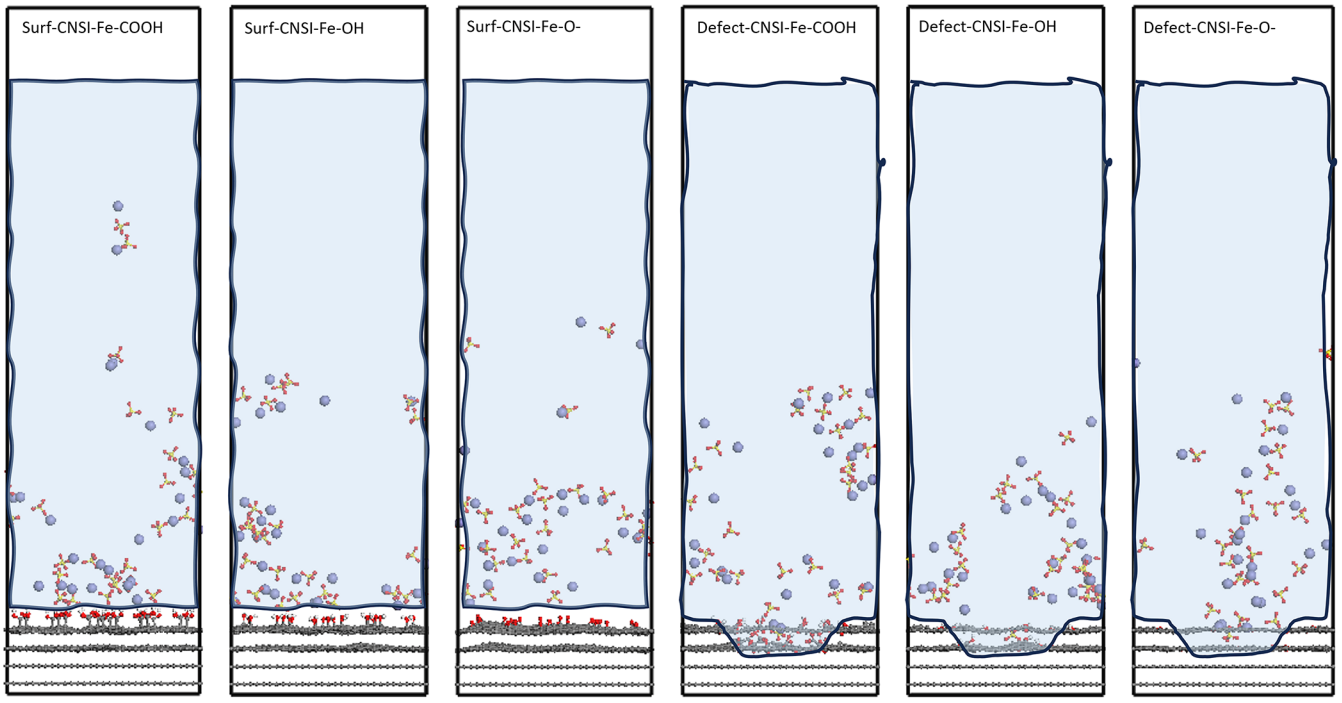

Figure 3. Snapshots of MD simulations for Surf−CNSI−Fe−COOH, Surf−CNSI−Fe−OH, Surf−CNSI−Fe−O−, defect−CNSI−Fe−COOH, defect−CNSI−Fe−OH, and defect−CNSI−Fe−O−.

values for the Temkin and Freundlich models reached 0.911 and 0.910, respectively. Additionally, the Freundlich parameter K_F (7.1859 $mg^{1+1/n}\cdot g^{-1}\cdot L^{-1/n}$), representing the adsorption capacity, was significantly larger than those for Cu^{2+} (0.8236 $mg^{1+1/n}\cdot g^{-1}\cdot L^{-1/n}$) and Zn^{2+} ions (0.1675 $mg^{1+1/n}\cdot g^{-1}\cdot L^{-1/n}$); parameter n, representing the adsorption strength, also exhibited this trend. Similarly, parameter A, representing binding capacity in the Temkin model, was also unusually large.[37,38] Since the q_m of CNSI toward Fe^{2+} falls between those of Cu^{2+} and Zn^{2+}, neither single-layer nor multilayer adsorption was suitable for Fe^{2+}. It was reasonable to conclude that Fe^{2+} delivery by CNSI involved a heterogeneous specific adsorption process.

Unraveling Fe^{2+} Adsorption of CNSI−Fe by MD Simulations. Many adsorbents with metal ion adsorption capacity are chemisorption.[39−44] It has been proposed that oxygen-containing groups play an important role, but almost none of them have addressed the specific atomic-level interactions involved. MD simulations are useful in exploring the details of Fe^{2+} chemisorption by CNSI. Figure 3 shows the snapshots of Surf−CNSI−Fe−OH, Surf−CNSI−Fe−O−, defect−CNSI−Fe−COOH, defect−CNSI−Fe−OH, and defect−CNSI−Fe−O− systems during the production run. The ions in the defect−CNSI−Fe systems seemed to be closer to the interface and more densely packed than those in the surface−CNSI−Fe system. Moreover, Fe^{2+} and SO_4^{2-} ions in the defect−CNSI−Fe−OH system appeared to be more tightly adsorbed to the interface than those in other systems. Furthermore, SO_4^{2-} ions were surrounded by Fe^{2+} ions, which in turn continued to adsorb SO_4^{2-}. As a result, Fe^{2+} tended to aggregate with Fe^{2+}, showing a tendency to form clusters.

The radial distribution function (RDF)[45] was first used to explore the commonalities between the surface and defect systems. Figure 4a,h shows that all the RDF curves between Fe^{2+} and O of oxidized groups had no peaks before 4 Å, indicating that Fe^{2+} did not directly coordinate to the oxygen-containing groups (OG) on the surface. The sharp peaks at 2.03 Å for Fe^{2+} vs O(H_2O) RDF curves (Figure 4b,i) meant that Fe^{2+} were strongly coordinated with the O of water. The RDF curves for Fe^{2+} vs O(SO_4^{2-}) (Figure 4c,k) exhibited three distinct peaks. The first peak at 2.48 Å represented Fe^{2+} coordinating with two Os in the SO_4^{2-}—bidentate coordination. The second peak at 3.13 Å indicated that Fe^{2+} coordinated with only a single O in the SO_4^{2-}—monodentate coordination. Furthermore, the intensity of the first peak was greater than that of the second peak, indicating that $FeSO_4$ was more prevalent in the bidentate form. This was basically consistent with the quantum mechanics calculations in Table S2, where the Fe−S distance in the bidentate coordination is 2.65 Å. It should be noted that the Fe−S distance in the monodentate coordination is 2.85 Å. The bidentate $FeSO_4$ complex had a lower energy and was more stable than the monodentate complex. The third peak at 4.48 Å represented the electrostatic interaction between solvated Fe^{2+} and SO_4^{2-}.

On the other hand, as shown in Figure 4d,j, all kinds of the oxygen-containing groups formed hydrogen bonds with water at 2.7 Å, indicating that the interface was solvated. In addition, the oxygen-containing groups −COOH and −OH (Figure 4e,l) also formed hydrogen bonds with the O atoms of SO_4^{2-}. Now, looking back at the first peak of the RDF curve for Fe−O(OG), which appeared between 4.1 and 4.5 Å, it might be inferred that the Fe^{2+} adsorption at the interface occurred through the formation of hydrogen bonds between the water or SO_4^{2-} coordinated with Fe^{2+} and the oxygen-containing groups. Finally, the Fe−Fe RDF curves (Figure 4f,l) showed a plateau between 5.0 and 8.0 Å, indicating that Fe^{2+} aggregation occurred. Since Fe^{2+} coordinated with the two O atoms of SO_4^{2-} simultaneously to reduce the Fe−Fe distance, Fe^{2+} compact clusters were formed.

https://doi.org/10.1021/acs.jpcc.5c05997
J. Phys. Chem. C 2025, 129, 22526−22537

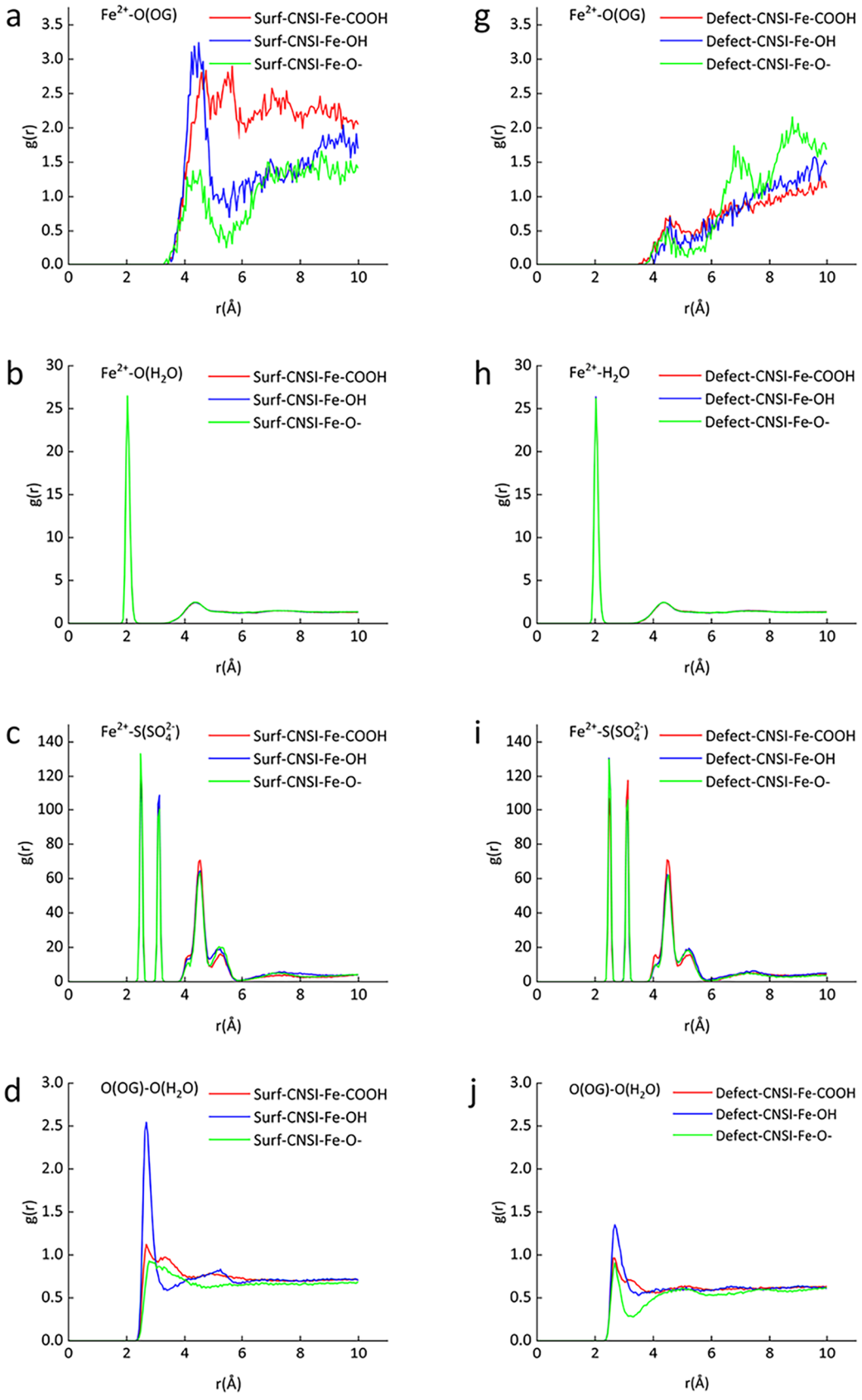

Figure 4. continued

https://doi.org/10.1021/acs.jpcc.5c05997
J. Phys. Chem. C 2025, 129, 22526−22537

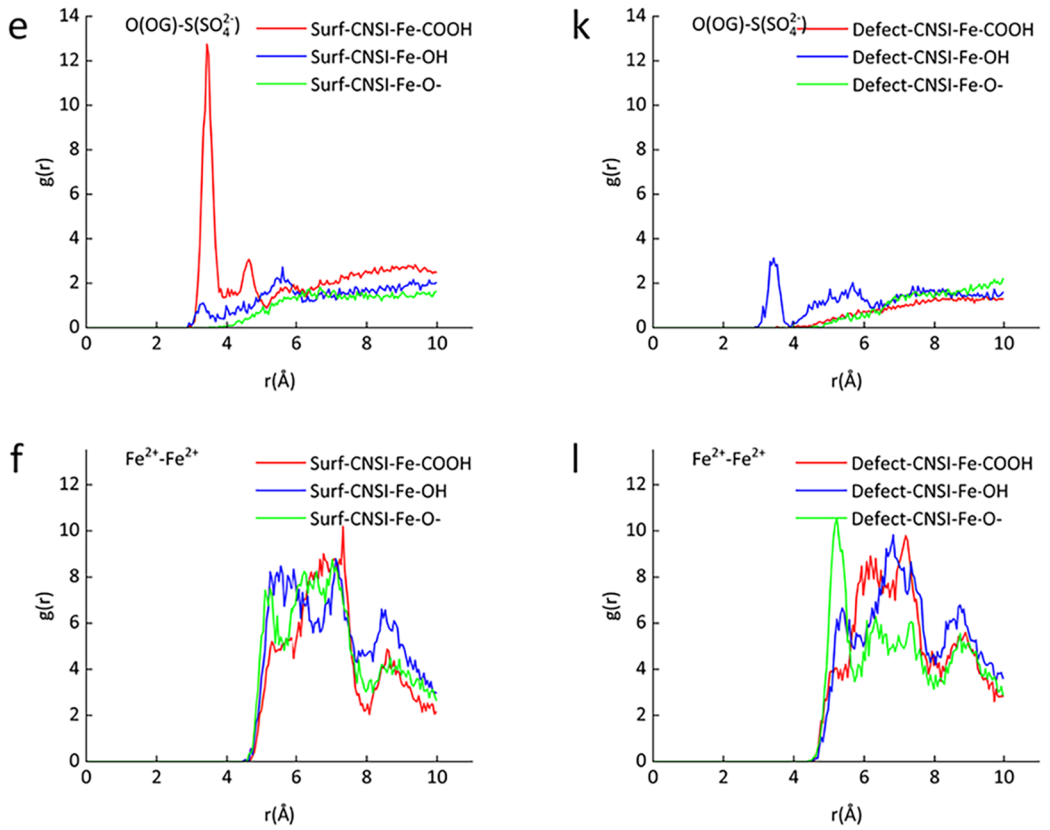

Figure 4. RDF curves of (a, g) Fe^{2+} vs O in oxygen-containing groups, (b, h) Fe^{2+} vs O in H_2O, (c, i) Fe^{2+} vs S in SO_4^{2-}, (d, j) O in oxygen-containing groups vs O in H_2O, (e, k) O in oxygen-containing groups vs S in SO_4^{2-}, and (f, l) Fe^{2+} vs Fe^{2+}, for Surf−CNSI−Fe and defect−CNSI−Fe systems.

Next, the MD analyses of different CNSI−Fe absorption were used to derive an intrinsic model for the adsorption of CNSI−Fe. For the three oxidation group systems in Figure 4d,j, the pair correlation function $g(r)$ of O(OG)−O(H_2O) was stronger for the OH system than for COOH and −O− in both the surface and defective systems. It indicated that OH formed the strongest hydrogen bonds with water, and its interface was most strongly solvated. Moreover, −OH and SO_4^{2-} were also hydrogen bonded, although the $g(r)$ of O(OG)−O(SO_4^{2-}) was most prominent in the Surf−CNSI−Fe−COOH system, and the other $g(r)$ functions showed no significant interactions in Figure 4e,k. Most notably, the $g(r)$ for Fe^{2+}−O(OG) was significantly smaller in the defect system than in the surface system, which seemed to be inconsistent with previous snapshots. This might suggest that $g(r)$ was not a determining factor of Fe^{2+} adsorption capacity.

Figure 5 shows the mean square displacement (MSD)[46] of particle Fe^{2+}, SO_4^{2-}, and H_2O in the surface and defect systems as a function of time, which better reflects the adsorption capacity of the interface for Fe^{2+}. First, the MSD profiles of Fe^{2+} and SO_4^{2-} looked very similar, indicating that the two were strongly correlated, including coordination and ionic interactions. Moreover, the MSD changes of both ions over time were much less than that of H_2O, which not only indicated the different diffusion rates but also suggested the adsorption of Fe^{2+} and SO_4^{2-} by CNSI. Second, the smaller the change in MSD over time, the less pronounced the particle diffusion and the stronger the adsorption of particles. Overall, the defect system exhibited stronger adsorption of particles, consistent with snapshots of the MD simulations (Figure 3). Furthermore, the contribution of oxygen-containing groups in the adsorption capacity followed the order: hydroxyl > epoxy > carboxyl. Therefore, it is inferred that the defect−CNSI−Fe−OH system was the primary model for Fe^{2+} adsorption by CNSI. Moreover, the reduction in O content in the CNSI suspension, in contrast to C40, suggests more hydroxyl or epoxy groups, which is beneficial to the adsorption of Fe^{2+} by CNSI.

Deciphering Fe^{2+} Delivery of CNSI−Fe in Comparison with Cu^{2+} and Zn^{2+}. With reference to adsorption experiments, MD analyses of the CNSI−Fe, CNSI−Cu, and CNSI−Zn systems were conducive to further elucidating the Fe^{2+} delivery mechanism of CNSI. Table 2 lists the diffusion coefficients (D)[47] of the three systems, i.e., the slopes of the MSD. The minimum diffusion coefficients of each particle for both surface and defect systems were examined, which were usually inversely correlated with adsorption capacity. The $D(Cu^{2+})$ value of 0.0220 $Å^2 \cdot ps^{-1}$ in surface−CNSI−Cu−COOH was smaller than the $D(Fe^{2+})$ value of 0.0325 $Å^2 \cdot ps^{-1}$ in surface−CNSI−Fe−O, which seemed to be consistent with the q_m relationship of Cu^{2+} and Fe^{2+}. However, the $D(SO_4^{2-})$ of the surface−CNSI−Cu−COOH system (0.0339 $Å^2 \cdot ps^{-1}$) was higher than that of the defect−CNSI−Fe−OH system (0.0308 $Å^2 \cdot ps^{-1}$). In addition, since the maximum adsorption capacity $q_m(Zn^{2+})$ is lowest among the three, theoretically, the diffusion coefficients $D(Zn^{2+})$ and $D(SO_4^{2-})$ of the CNSI−Zn system should be greater than those of CNSI−Cu and CNSI−Fe systems. But this is not the case. These results were inconsistent with the experimental q_m relationship of the three metal ions.

https://doi.org/10.1021/acs.jpcc.5c05997
J. Phys. Chem. C 2025, 129, 22526−22537

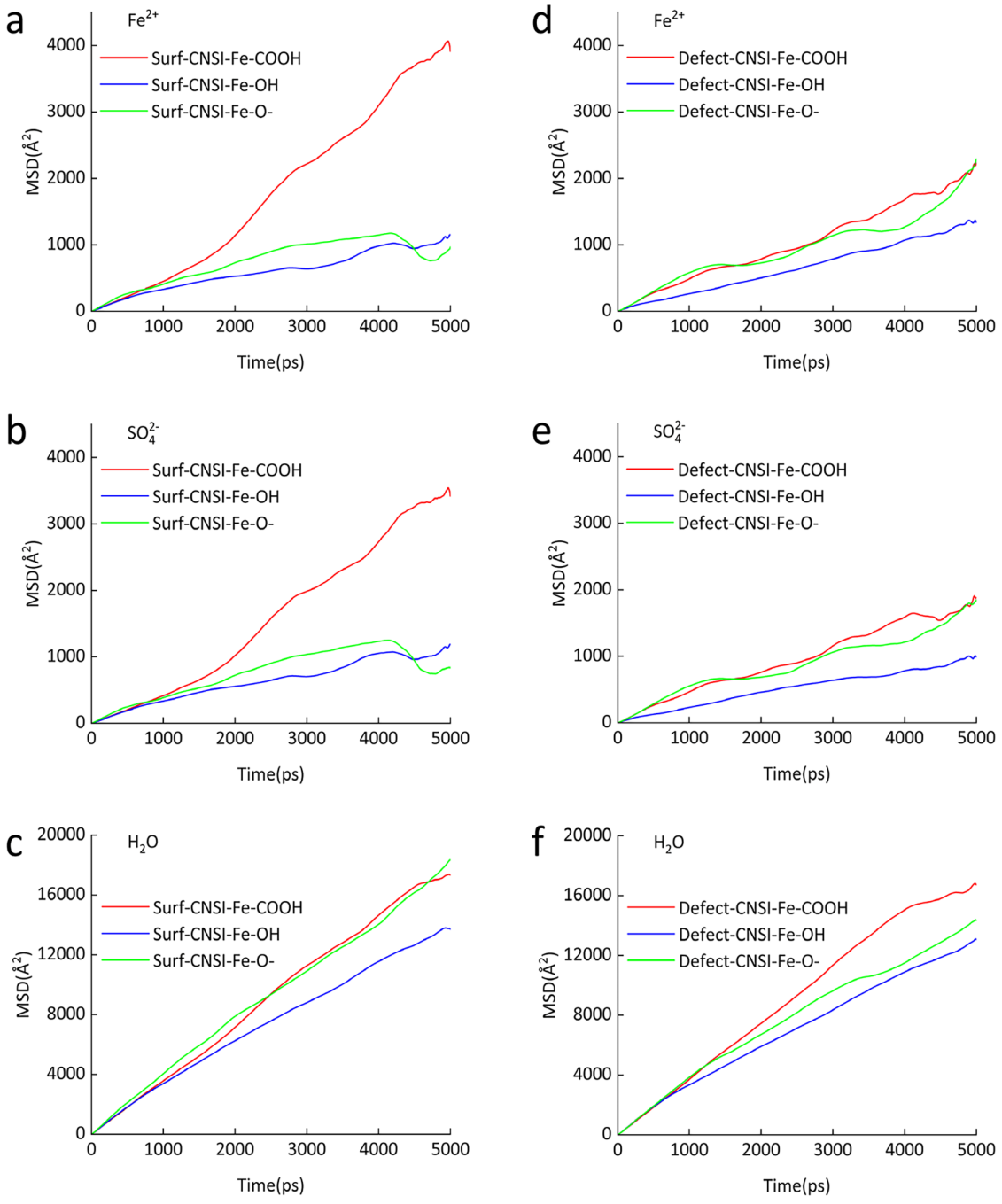

Figure 5. MSD diagrams in different CNSI−Fe systems for the particle: (a, d) Fe^{2+}, (b, e) SO_4^{2-}, and (c, f) H_2O.

Given the multilayer adsorption of Cu^{2+}, the possible cluster adsorption of Fe^{2+}, and the single-layer adsorption phenomenon of Zn^{2+} as analyzed above, the diffusion coefficients of the ions here, representing average values, were therefore not suitable for correlating with the total value q_m. MD analysis of the CNSI−Fe system demonstrated that metal ion adsorption primarily occurred through the formation of hydrogen bonds between coordination water and oxygen-containing groups. Although $D(H_2O)$ was significantly larger than $D(M^{2+})$ and $D(SO_4^{2-})$ due to bulk water diffusion, the amount of bound water around different metals varied, resulting in different diffusion coefficients. Therefore, $D(H_2O)$ should be correlated to the adsorption capacities of metal ions. Comparing the minimum diffusion coefficients of water for the three metal ion systems, which were 0.4173 $Å^2 \cdot ps^{-1}$ (defect−CNSI−Cu−COOH) < 0.4214 $Å^2 \cdot ps^{-1}$ (defect−CNSI−Fe−OH) < 0.4590 $Å^2 \cdot ps^{-1}$ (defect−CNSI−Zn−COOH); this was fully consistent with the experimental q_m relationship. Meanwhile, this also indicated that defect adsorption was the primary source of metal ion adsorption by CNSI, which aligned with the mesoporous characteristics of C40 as the CNSI raw material (Figure 2). Therefore, the defect−CNSI−Cu−COOH and defect−CNSI−Zn−COOH systems should be the primary models for Cu^{2+} and Zn^{2+} adsorption by CNSI.

Next, the defect−CNSI−Fe−OH, defect−CNSI−Cu−COOH, and defect−CNSI−Zn−COOH systems were used for further analysis. As shown in the RDF plots for the three metals in Figure 6a−c, similar to Fe^{2+}, Zn^{2+} and Cu^{2+} did not

https://doi.org/10.1021/acs.jpcc.5c05997
J. Phys. Chem. C 2025, 129, 22526−22537

Table 2. Diffusion Coefficients of Particles in CNSI−Metal Systems[a]

	$D(M^{2+})$		$D(SO_4^{2-})$		$D(H_2O)$	
	surface	defect	surface	defect	surface	defect
CNSI−Fe−COOH	0.1446	0.0668	0.1267	0.0591	0.6077	0.5931
CNSI−Cu−COOH	0.0220	0.0367	0.0339	0.0343	0.5286	0.4173
CNSI−Zn−COOH	0.0297	0.0805	0.0229	0.0859	0.5604	0.4590
CNSI−Fe−OH	0.0333	0.0443	0.0354	0.0308	0.4530	0.4214
CNSI−Cu−OH	0.0877	0.1410	0.0998	0.1509	0.5885	0.4545
CNSI−Zn−OH	0.0339	0.0726	0.0309	0.0573	0.4605	0.4977
CNSI−Fe−O−	0.0325	0.0554	0.0346	0.0495	0.5800	0.4546
CNSI−Cu−O−	0.0370	0.2653	0.0374	0.2527	0.4665	0.8960
CNSI−Zn−O−	0.0347	0.0382	0.0389	0.0377	0.5393	0.5001

[a]Unit: $Å^2 \cdot ps^{-1}$; M = Fe, Cu, and Zn.

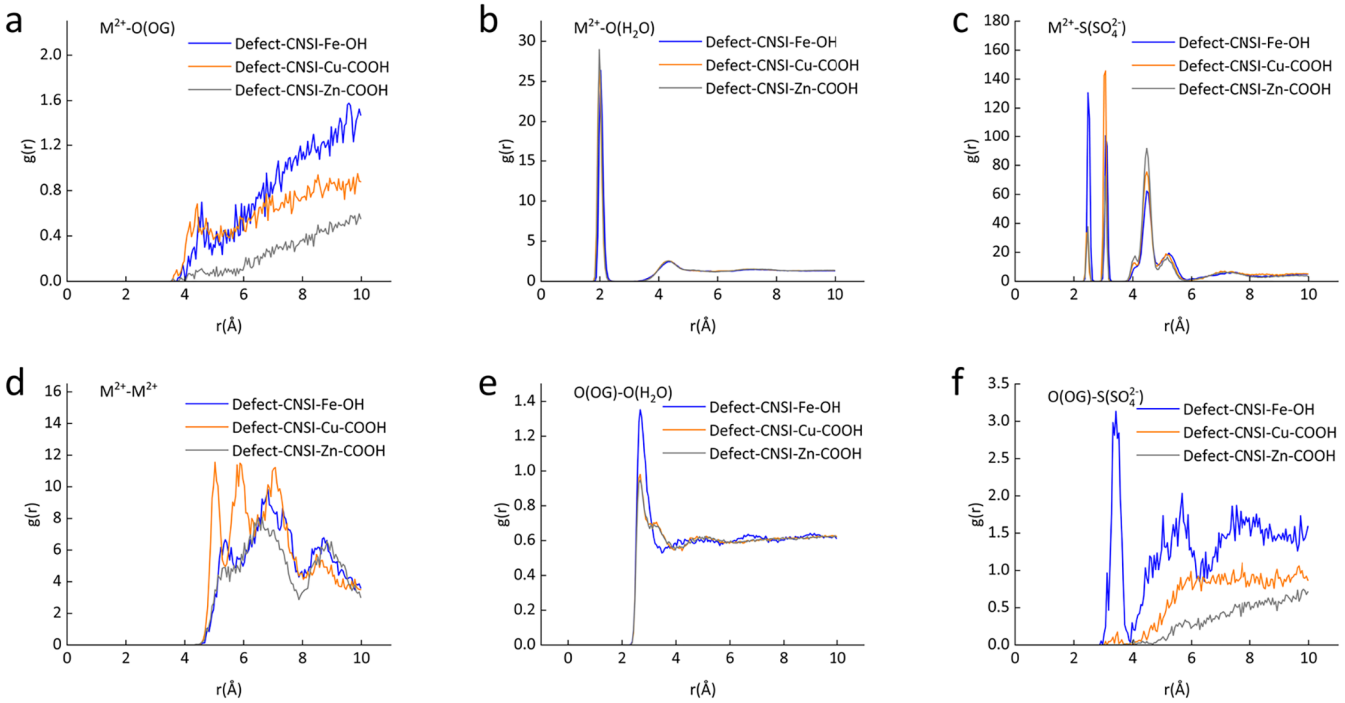

Figure 6. RDF curves of (a) M^{2+} vs O in oxygen-containing groups, (b) M^{2+} vs O in H_2O, (c) M^{2+} vs S in SO_4^{2-}, (d) M^{2+} vs M^{2+}, (e) O in oxygen-containing groups vs O in H_2O, (f) O in oxygen-containing groups vs S in SO_4^{2-}, for defect−CNSI−Fe systems, and M^{2+} for Fe^{2+}, Cu^{2+}, and Zn^{2+}.

directly coordinate with the oxygen-containing groups in the interface but strongly coordinated with H_2O SO_4^{2-}. However, unlike Fe^{2+}, the RDF curves of Zn^{2+}−$O(SO_4^{2-})$ and Cu^{2+}−$S(SO_4^{2-})$ in Figure 6c showed that the intensity of the first bidentate coordination peak was not only smaller than that of the second monodentate coordination peak but also significantly smaller than that of Fe^{2+}. This indicated that $ZnSO_4$ and $CuSO_4$ in aqueous solutions, unlike $FeSO_4$, exhibited more stable monodentate coordination forms than the bidentate coordination ones, consistent with density functional theory (DFT) calculations (Table S2). This could also be inferred that Zn^{2+} and Cu^{2+} were less likely to form tight clusters like Fe^{2+}.

On the other hand, Figure 6d shows that the RDF curve of Cu^{2+}−Cu^{2+} had three distinct equidistant peaks, indicating that Cu^{2+} ions were spatially arranged in an orderly manner like crystal characteristics. This perfectly explained the conclusion of the adsorption experiment that Cu^{2+} was adsorbed by CNSI in a multiple-layered form. Additionally, the second peak of the Cu^{2+}−$S(SO_4^{2-})$ RDF curve in Figure 6c was significantly stronger than the other two ions, suggesting that the strong monodentate coordination between Cu^{2+} and SO_4^{2-} was the key for multilayer adsorption. However, for Zn^{2+}, the unstable bidentate structure made it difficult to form tight clusters, and the weak monodentate coordination also hindered the multilayer adsorption. The last column of Table S2 shows the coordination energies of the three metal ion complexes. The monodentate coordination of hydrated $CuSO_4$ was the strongest; therefore, it was easy to form multilayer adsorption. Considering that the monodentate coordination of $ZnSO_4$ was also the weakest, although Figure 6d shows that Zn^{2+} formed a platform structure like Fe^{2+}, Zn^{2+} ions could only loosely pile up rather than form clusters.

In Figure 6e, the O(OG)−$O(H_2O)$ RDF curves of all three metal ion systems exhibited strong peaks at approximately 2.68 Å, indicating that the adsorption of metal ions by CNSI was achieved through the formation of hydrogen bonds between the oxygen-containing groups at the interface and coordinated water. However, as shown in Figure 6f, only the O(OG)−$S(SO_4^{2-})$ RDF curve of the defect−CNSI−Fe−OH system had

https://doi.org/10.1021/acs.jpcc.5c05997
J. Phys. Chem. C 2025, 129, 22526−22537

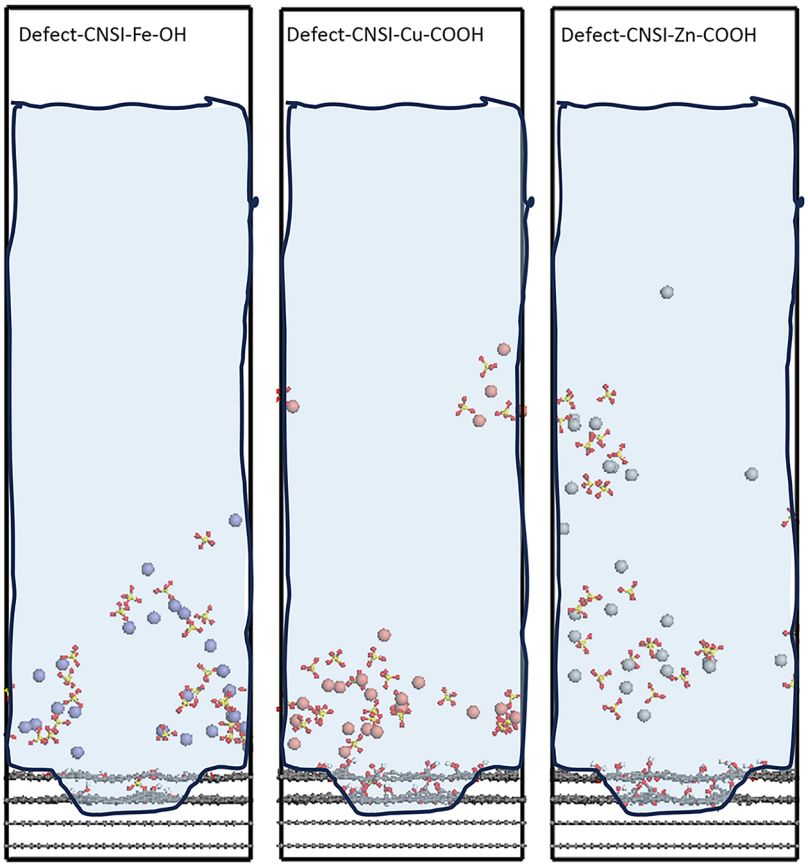

Figure 7. Snapshots of MD simulations for defect−CNSI−Fe−OH, defect−CNSI−Cu−COOH, and defect−CNSI−Zn−COOH.

a strong peak at approximately 3.42 Å because Fe^{2+} readily formed a dense cluster structure due to the bidentate coordination with SO_4^{2-}. Therefore, with SO_4^{2-} located on the outer layer of the cluster structure, the Fe^{2+} adsorption by CNSI could also be strengthened through the formation of hydrogen bonds between SO_4^{2-} and OH groups at the interface. Moreover, this interaction facilitated the O(OG)−O(H_2O) interaction, explaining that the $g(r)$ value was higher for the defect−CNSI−Fe−OH system in Figure 6e. This further validated the cluster-mediated Fe^{2+} delivery mechanism in CNSI−Fe.

Furthermore, the MD snapshot in Figure 7 showed that Zn^{2+} in the defect−CNSI−Zn−COOH system was loosely distributed at the interface, exhibiting the weakest adsorption by CNSI. In contrast, in the defect−CNSI−Cu−COOH system, most Cu^{2+} ions were more tightly bound to the interface, indicating the largest q_m by CNSI. Further observation revealed that there were identifiable continuous SO_4^{2-} or Cu^{2+} ions to form layers with the characteristics of multilayer adsorption. In defect−CNSI−Fe−OH, SO_4^{2-} and Fe^{2+} were alternately distributed with a tendency to form clusters. All these findings were consistent with experimental results. Therefore, by comparison with Cu^{2+} and Zn^{2+}, the special cluster-mediated Fe^{2+} delivery mechanism of CNSI−Fe was fully revealed.

CONCLUSIONS

In summary, this study investigated the Fe^{2+} delivery mechanism through CNSI (CNSI−Fe system) by using adsorption experiments and MD simulations in comparison with those of CNSI−Cu and CNSI−Zn systems. The adsorption of the three metal ions by CNSI was chemisorption with maximum adsorption capacities $q_m(Cu^{2+}) > q_m(Fe^{2+}) > q_m(Zn^{2+})$. CNSI−Cu exhibited heterogeneous multilayer adsorption characteristics, and CNSI−Zn included heterogeneous single-layer adsorption characteristics, but the adsorption characteristics of CNSI−Fe could not be simply described. Defect−CNSI−Fe−OH, defect−CNSI−Cu−COOH, and defect−CNSI−Zn−COOH systems served as the primary delivery models for Fe^{2+}, Cu^{2+}, and Zn^{2+} by CNSI, which were aligned with the mesoporous characteristics of CNSI materials. All metal ions are coordinated with H_2O and SO_4^{2-}. Cu^{2+} and Zn^{2+} primarily formed monodentate coordination of SO_4^{2-}, which resulted in multilayer adsorption for CNSI−Cu and loosely packed structures resembling single-layer adsorption for CNSI−Zn. In contrast, Fe^{2+} formed bidentate coordination with SO_4^{2-}, facilitating the formation of tightly clustered structures, which explained the q_m relationship of CNSI toward these three metal ions observed experimentally. On the other hand, MD analyses indicated that the adsorption of all metal ions by CNSI depended on the formation of hydrogen bonds between the oxygen-containing groups of CNSI and the water coordinated with metal ions. Unlike the adsorption of Cu^{2+} and Zn^{2+} ions, the cluster characteristics of CNSI−Fe exposing SO_4^{2-} on the outer layer and the hydrogen bonding between SO_4^{2-} and the oxygen-containing groups of CNSI also contributed to its adsorption, making the CNSI−Fe system so special. This provided a comprehensive atomic-level explanation for the chemisorption of Fe^{2+} by the CNSI.

In conclusion, the cluster-mediated Fe^{2+} delivery mechanism, mainly due to the acidic formula and mesoporous

https://doi.org/10.1021/acs.jpcc.5c05997
J. Phys. Chem. C 2025, 129, 22526−22537

characteristics of CNSI, is beneficial for enhancing adsorption in CNSI suspensions with more hydroxyl or epoxy groups. Meanwhile, its adsorption strength and kinetic characteristics would also be conducive to the release of Fe^{2+} in ferroptosis therapy. It is hoped that our study would benefit the understanding of CNSI−Fe at the molecular level and accelerate its clinical applications of ferroptosis-based cancer therapy.

■ ASSOCIATED CONTENT

Supporting Information

The Supporting Information is available free of charge at https://pubs.acs.org/doi/10.1021/acs.jpcc.5c05997.

Additional experimental results; additional MD simulation results; and additional QM calculation results (PDF)

■ AUTHOR INFORMATION

Corresponding Authors

Junxian Chen − *Key Laboratory of General Chemistry of the National Ethnic Affairs Commission, School of Chemistry and Environment, Southwest Minzu University, Chengdu 610041, China*; orcid.org/0000-0002-2067-8340; Email: chenjunxian@swun.edu.cn

Sheng-Tao Yang − *Key Laboratory of General Chemistry of the National Ethnic Affairs Commission, School of Chemistry and Environment, Southwest Minzu University, Chengdu 610041, China*; Email: yangst@swun.edu.cn

Xiaohai Tang − *Sichuan Enray Pharmaceutical Sciences Company, Chengdu 610041, China*; Email: pharmmateceo@enraypharm.com

Authors

Shiga Jila − *Key Laboratory of General Chemistry of the National Ethnic Affairs Commission, School of Chemistry and Environment, Southwest Minzu University, Chengdu 610041, China*

Cheng Zeng − *Sichuan Enray Pharmaceutical Sciences Company, Chengdu 610041, China*

Kexin Tang − *Sichuan Enray Pharmaceutical Sciences Company, Chengdu 610041, China*

Ping Xie − *Sichuan Enray Pharmaceutical Sciences Company, Chengdu 610041, China*

Huahui Yuan − *Sichuan Enray Pharmaceutical Sciences Company, Chengdu 610041, China*

Chunchun Zhang − *Analytical & Testing Center, Sichuan University, Chengdu, Sichuan 610064, China*

Complete contact information is available at: https://pubs.acs.org/10.1021/acs.jpcc.5c05997

Author Contributions

‖S.J. and C.Z. contributed equally. S.J.: Investigation and writing—original draft. C. Z.: Investigation and writing—original draft. K. T.: Methodology; P.X.: Methodology and project administration. C. Z.: Investigation. H.Y.: Methodology. J.C.: Conceptualization, writing—review and editing, supervision, and funding acquisition. S.-T.Y.: Conceptualization, writing—review and editing, and funding acquisition. X.T.: Conceptualization, writing—review and editing, and supervision. All authors contributed to manuscript revision, read, and approved the submitted version.

Notes

The authors declare no competing financial interest.

■ ACKNOWLEDGMENTS

We acknowledge financial support from the Science & Technology Department of Sichuan Province (No. 2023JDRC0014) and the Fundamental Research Funds for the Central Universities, Southwest Minzu University (No. ZYN2024071).

■ REFERENCES

(1) Wang, J.; Sun, Z.; Wang, S.; Zhao, C.; Xu, J.; Gao, S.; Yang, M.; Sheng, F.; Gao, S.; Hou, Y. Biodegradable ferrous sulfide-based nanocomposites for tumor theranostics through specific intratumoral acidosis-induced metabolic symbiosis disruption. *J. Am. Chem. Soc.* **2022**, *144* (43), 19884−19895.

(2) Liang, H.; Wu, X.; Zhao, G.; Feng, K.; Ni, K.; Sun, X. Renal clearable ultrasmall single-crystal Fe nanoparticles for highly selective and effective ferroptosis therapy and immunotherapy. *J. Am. Chem. Soc.* **2021**, *143* (38), 15812−15823.

(3) He, T.; Yuan, Y.; Jiang, C.; Blum, N. T.; He, J.; Huang, P.; Lin, J. Light-triggered transformable ferrous ion delivery system for photothermal primed chemodynamic therapy. *Angew. Chem.* **2021**, *133* (11), 6112−6119.

(4) Li, Z.; Wu, X.; Wang, W.; Gai, C.; Zhang, W.; Li, W.; Ding, D. Fe (II) and tannic acid-cloaked MOF as carrier of artemisinin for supply of ferrous ions to enhance treatment of triple-negative breast cancer. *Nanoscale Res. Lett.* **2021**, *16*, No. 37.

(5) Hashemi, B.; Rezania, S. Carbon-based sorbents and their nanocomposites for the enrichment of heavy metal ions: a review. *Microchim. Acta* **2019**, *186*, No. 578.

(6) Li, Z.; Ao, S.; Bu, Z.; Wu, A.; Wu, X.; Shan, F.; Ji, X.; Zhang, Y.; Xing, Z.; Ji, J. Clinical study of harvesting lymph nodes with carbon nanoparticles in advanced gastric cancer: a prospective randomized trial. *World J. Surg. Oncol.* **2016**, *14*, No. 88.

(7) Xie, P.; Xin, Q.; Yang, S.-T.; He, T.; Huang, Y.; Zeng, G.; Ran, M.; Tang, X. Skeleton labeled 13C-carbon nanoparticles for the imaging and quantification in tumor drainage lymph nodes. *Int. J. Nanomed.* **2017**, 4891−4899.

(8) Xie, P.; Yang, S.-T.; He, T.; Yang, S.; Tang, X.-H. Bioaccumulation and toxicity of carbon nanoparticles suspension injection in intravenously exposed mice. *Int. J. Mol. Sci.* **2017**, *18* (12), 2562.

(9) Tian, Y.; Lin, Y.; Guo, H.; Hu, Y.; Li, Y.; Fan, L.; Zhao, X.; Wang, D.; Tan, B.; Zhao, Q. Safety and efficacy of carbon nanoparticle suspension injection and indocyanine green tracer-guided lymph node dissection during robotic distal gastrectomy in patients with gastric cancer. *Surg. Endosc.* **2022**, *36*, 3209.

(10) Huang, Y.; Zeng, G.; Xin, Q.; Yang, J.; Zeng, C.; Tang, K.; Yang, S. T.; Tang, X. Carbon nanoparticles suspension injection for photothermal therapy of xenografted human thyroid carcinoma in vivo. *MedComm* **2020**, *1* (2), 202−210.

(11) Huang, Y.; Xie, P.; Yang, S.-T.; Zhang, X.; Zeng, G.; Xin, Q.; Tang, X.-H. Carbon nanoparticles suspension injection for the delivery of doxorubicin: comparable efficacy and reduced toxicity. *Mater. Sci. Eng., C* **2018**, *92*, 416−423.

(12) Xie, P.; Tang, X.; Li, L.; Qian, Z.; Ran, M.; Zhang, X.; Xin, Q.; Luo, H. Drug-loaded carbon nanoparticle suspension injection: drug selection, releasing behavior, in vitro cytotoxicity and in vivo lymph node targeting. *J. Nanosci. Nanotechnol.* **2016**, *16* (7), 6910−6918.

(13) Yang, Q.; Wang, X.-d.; Chen, J.; Tian, C.-x.; Li, H.-j.; Chen, Y.-j.; Lv, Q. A clinical study on regional lymphatic chemotherapy using an activated carbon nanoparticle−epirubicin in patients with breast cancer. *Tumor Biol.* **2012**, *33*, 2341−2348.

(14) Xie, P.; Yang, S.-T.; Huang, Y.; Zeng, C.; Xin, Q.; Zeng, G.; Yang, S.; Xia, P.; Tang, X.; Tang, K. Carbon nanoparticles−Fe (II) complex for efficient tumor inhibition with low toxicity by amplifying

oxidative stress. *ACS Appl. Mater. Interfaces* **2020**, *12* (26), 29094−29102.
(15) Xie, P.; Huang, Y.; Tang, K.; Wu, X.; Zeng, C.; Yang, S.-T.; Tang, X. Carbon nanoparticles-Fe (II) complex for efficient theranostics of xenografted colonic tumor. *Cancer Nanotechnol* **2023**, *14* (1), No. 38.
(16) Liu, Y.; Zou, Y.; Zhu, H.; Xie, S.; Wu, J.; Li, J.; Li, J. Effect of inhomogeneous structure on the water desalination performance of graphitic carbon nitride nanochannels: A molecular dynamics study. *J. Mol. Liq.* **2024**, *396*, No. 123953.
(17) Wang, P.; Li, W.; Du, C.; Zheng, X.; Sun, X.; Yan, Y.; Zhang, J. CO2/N2 separation via multilayer nanoslit graphene oxide membranes: Molecular dynamics simulation study. *Comput. Mater. Sci.* **2017**, *140*, 284−289.
(18) Tang, H.; Zhao, Y.; Shan, S.; Yang, X.; Liu, D.; Cui, F.; Xing, B. Theoretical insight into the adsorption of aromatic compounds on graphene oxide. *Environ. Sci. Nano* **2018**, *5* (10), 2357−2367.
(19) Hou, D.; Zhang, Q.; Wang, M.; Zhang, J.; Wang, P.; Ge, Y. Molecular dynamics study onwater and ions on the surface of graphene oxide sheet: Effects of functional groups. *Comput. Mater. Sci.* **2019**, *167*, 237−247.
(20) Ho, Y.-S.; Mckay, G. Kinetic models for the sorption of dye from aqueous solution by wood. *Process Saf. Environ. Prot.* **1998**, *76* (2), 183−191.
(21) Ho, Y.-S.; McKay, G. Pseudo-second order model for sorption processes. *Process Biochem.* **1999**, *34* (5), 451−465.
(22) Asgari, G.; Roshani, B.; Ghanizadeh, G. The investigation of kinetic and isotherm of fluoride adsorption onto functionalize pumice stone. *J. Hazard. Mater.* **2012**, *217−218*, 123−132.
(23) Yang, C.-h. Statistical mechanical study on the Freundlich isotherm equation. *J. Colloid Interface Sci.* **1998**, *208* (2), 379−387.
(24) Chu, K. H. Revisiting the Temkin isotherm: dimensional inconsistency and approximate forms. *Ind. Eng. Chem. Res.* **2021**, *60* (35), 13140−13147.
(25) Qiu, L.; Yang, X.; Gou, X.; Yang, W.; Ma, Z. F.; Wallace, G. G.; Li, D. Dispersing carbon nanotubes with graphene oxide in water and synergistic effects between graphene derivatives. *Chem. - Eur. J.* **2010**, *16* (35), 10653−10658.
(26) Sun, H. COMPASS: an ab initio force-field optimized for condensed-phase applications overview with details on alkane and benzene compounds. *J. Phys. Chem. B* **1998**, *102* (38), 7338−7364.
(27) Clark, S. J.; Segall, M. D.; Pickard, C. J.; Hasnip, P. J.; Probert, M. I.; Refson, K.; Payne, M. C. First principles methods using CASTEP. *Z. Kristallogr. - Cryst. Mater.* **2005**, *220* (5−6), 567−570.
(28) Berendsen, H. J. C.; Postma, J. V.; Van Gunsteren, W. F.; DiNola, A.; Haak, J. R. Molecular dynamics with coupling to an external bath. *J. Chem. Phys.* **1984**, *81* (8), 3684−3690.
(29) Karasawa, N.; Goddard III, W. A. Acceleration of convergence for lattice sums. *J. Phys. Chem. A* **1989**, *93* (21), 7320−7327.
(30) Michalak, I.; Chojnacka, K.; Witek-Krowiak, A. State of the art for the biosorption process—a review. *Appl. Biochem. Biotechnol.* **2013**, *170*, 1389−1416.
(31) Lucaci, A. R.; Bulgariu, D.; Ahmad, I.; Bulgariu, L. Equilibrium and kinetics studies of metal ions biosorption on alginate extracted from marine red algae biomass (Callithamnion corymbosum sp.). *Polymers* **2020**, *12* (9), 1888.
(32) Webb, P. A.; Orr, C. *Analytical Methods in Fine Particle Technology*; Micromeritics Instrument Corporation, 1997.
(33) Summers, M.; Oh, J.; Lungu, C. T. Determination of activated carbon fiber adsorption capacity for several common organic vapors: applications for respiratory protection. *J. Air Waste Manage. Assoc.* **2022**, *72* (6), 570−580.
(34) Hemmati, N.; Tabzar, A.; Ghazanfari, M. H. Adsorption of sodium dodecyl benzene sulfonate onto carbonate rock: kinetics, equilibrium and mechanistic study. *J. Dispersion Sci. Technol.* **2018**, *39* (5), 687−699.
(35) Bansal, R. C.; Goyal, M. *Activated Carbon Adsorption*; CRC Press, 2005.
(36) Samarghandi, M.; Hadi, M.; Moayedi, S.; Askari, F. B. Two-parameter isotherms of methyl orange sorption by pinecone derived activated carbon. *J. Environ. Health Sci. Eng.* **2009**, *6* (4), 285−294.
(37) Ayawei, N.; Ebelegi, A. N.; Wankasi, D. Modelling and interpretation of adsorption isotherms. *J. Chem.* **2017**, *2017* (1), No. 3039817.
(38) Batool, F.; Akbar, J.; Iqbal, S.; Noreen, S.; Bukhari, S. N. A. Study of isothermal, kinetic, and thermodynamic parameters for adsorption of cadmium: an overview of linear and nonlinear approach and error analysis. *Bioinorg. Chem. Appl.* **2018**, *2018* (1), No. 3463724.
(39) Zinicovscaia, I.; Yushin, N.; Humelnicu, D.; Grozdov, D.; Ignat, M.; Demcak, S.; Humelnicu, I. Sorption of Ce (III) by silica SBA-15 and titanosilicate ETS-10 from aqueous solution. *Water* **2021**, *13* (22), 3263.
(40) Zhang, M.; Yin, Q.; Ji, X.; Wang, F.; Gao, X.; Zhao, M. High and fast adsorption of Cd (II) and Pb (II) ions from aqueous solutions by a waste biomass based hydrogel. *Sci. Rep.* **2020**, *10* (1), No. 3285.
(41) Youssif, M. M.; El-Attar, H. G.; Hessel, V.; Wojnicki, M. Recent Developments in the Adsorption of Heavy Metal Ions from Aqueous Solutions Using Various Nanomaterials. *Materials* **2024**, *17* (21), 5141.
(42) Özkan, B.; Altaş, Y.; İnan, S. Selective adsorption of actinides and rare earth elements from leach liquor using metal oxide-polymer nanocomposites. *J. Radioanal. Nucl. Chem.* **2024**, *333* (11), 5777−5790.
(43) Macena, M.; Pereira, H.; Cruz-Lopes, L.; Grosche, L.; Esteves, B. Competitive adsorption of metal ions by lignocellulosic materials: A review of applications, mechanisms and influencing factors. *Separations* **2025**, *12* (3), 70.
(44) Qin, J.; Fang, Y.; Ou, C.; Wang, J.; Huang, F.; Wen, Q.; Liao, Z.; Shi, J. Highly efficient Cd2+ and Cu2+ removal by MgO-modified tobermorite in aqueous solutions. *J. Environ. Chem. Eng.* **2023**, *11* (2), No. 109534.
(45) Maron, J.; Winokur, M.; Mattes, B. Processing-induced changes in the local structure of amorphous polyaniline by radial distribution function analysis of X-ray scattering data. *Macromolecules* **1995**, *28* (13), 4475−4486.
(46) Chandrasekhar, S. Stochastic problems in physics and astronomy. *Rev. Mod. Phys.* **1943**, *15* (1), 1.
(47) Tang, C.; Ding, K.; Liu, Y.; Yu, S.; Chen, J.; Feng, X.; Zhang, C.; Chen, J. Quantitative relationship between the structures and properties of VOCs and SOA formation on the surfaces of acidic aerosol particles. *Phys. Chem. Chem. Phys.* **2021**, *23* (21), 12360−12370.

https://doi.org/10.1021/acs.jpcc.5c05997
J. Phys. Chem. C 2025, 129, 22526−22537